Reducing honeycomb-generated turbulence with a passive grid

Experiments in Fluids (2023) 64:127
https://doi.org/10.1007/s00348-023-03669-w

RESEARCH ARTICLE

Reducing honeycomb-generated turbulence with a passive grid

N. R. M. Schipper[1] · J. G. M. Kuerten[1] · J. C. H. Zeegers[2]

Received: 12 January 2023 / Revised: 31 May 2023 / Accepted: 15 June 2023

Abstract
Honeycombs are widely used to laminarize fluid streams by inhibiting the lateral components of the fluctuating velocity. However, they also produce additional turbulence by themselves due to the formation of large-scale instabilities and the breakup of the individual velocity profiles stemming from the honeycomb cells. In the present research, we use 2D-planar particle image velocimetry to study how honeycomb-generated turbulence is affected by a downstream grid. It is found that placing a grid near the honeycomb discharge drastically enhances flow uniformity by separating the strong jets stemming from the individual honeycomb cells into many smaller jets that are much more rapidly dissipated. The results show that using a grid reduces the integral length scale by up to a factor 10, and the axial and lateral energy spectra reveal that the grid primarily limits the energy contained in eddies with lower wave numbers. Furthermore, the grid can reduce the magnitude of peak turbulence intensity by as much as 95% and leads to a large reduction of the correlation length, as long as it is positioned upstream of the onset of the large-scale honeycomb-induced instabilities. A downstream grid is highly beneficial for both a laminar and turbulent honeycomb discharge and is most effective when there is a slight offset between the grid and honeycomb. Even though longer honeycombs generally produce more turbulence than short ones due to the larger length-scale of the shear layers, these effects are almost entirely decoupled when using a honeycomb-grid combination. Finally, a honeycomb-grid combination effectively inhibits both axial and lateral turbulence.

J. G. M. Kuerten and J. C. H. Zeegers have equally contributed to this work.

✉ N. R. M. Schipper
n.r.m.schipper@tue.nl

J. G. M. Kuerten
j.g.m.kuerten@tue.nl

J. C. H. Zeegers
j.c.h.zeegers@tue.nl

[1] Department of Mechanical Engineering, Eindhoven University of Technology, P.O. Box 513, 5600 MB Eindhoven, The Netherlands

[2] Department of Applied Physics, Eindhoven University of Technology, P.O. Box 513, 5600 MB Eindhoven, The Netherlands

Published online: 03 July 2023

Graphic abstract

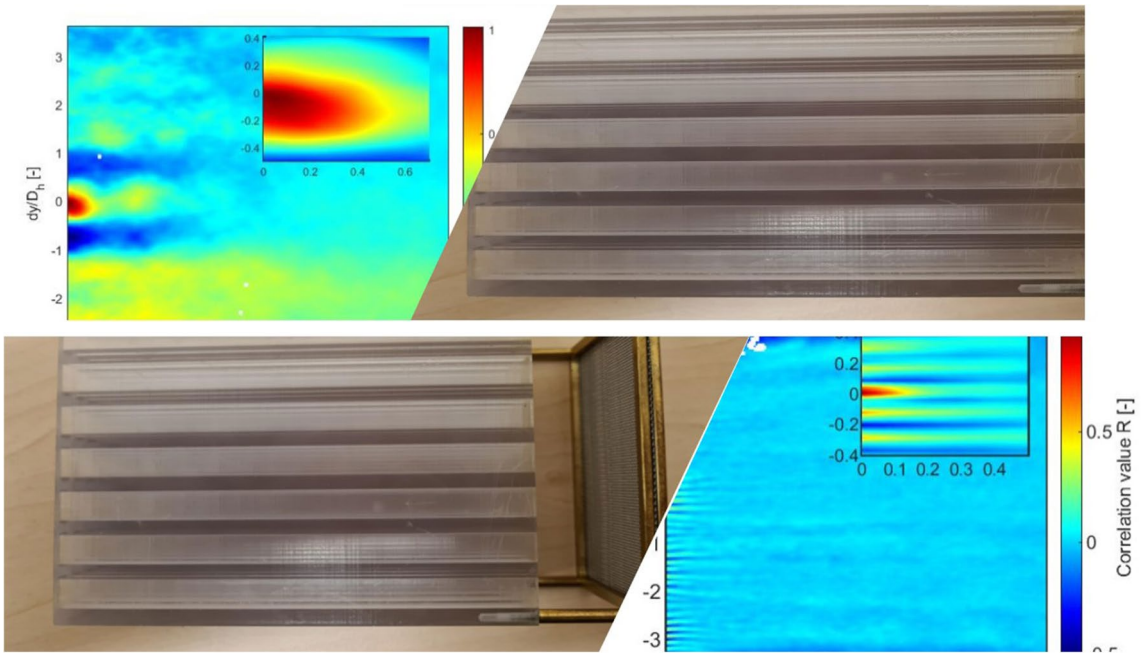

1 Introduction

Honeycombs are an essential tool to enhance flow quality and limit turbulence production in many industrial processes and scientific research. For instance, they are utilized to improve segregation performance in magnetic density separation (MDS) (Tajfirooz et al. 2021) and for controlling free-stream wind (Mikhailova et al. 1994) and water tunnel (Lumley and McMahon 1967) turbulence. Honeycombs are particularly effective for reducing large-scale swirling fluid motion (Farell and Youssef 1996) and prevent the uncontrollable growth of turbulence by inhibiting the lateral components of the fluctuating velocity (Loehrke and Nagib 1976). However, despite reducing the turbulence level of the feed stream, honeycombs may produce new vigorous turbulence near their discharge due to the formation of large-scale instabilities and the breakup of the individual velocity profiles stemming from the honeycomb cells (Thijs et al. 2021). In spite of the extensive research on turbulence suppression by honeycombs, studies on methods to reduce the turbulence generated by honeycombs are lacking. A few studies have shown that honeycomb-generated turbulence is strongly correlated with honeycomb length (Schipper 2022; Loehrke and Nagib 1976) and some suggested that positioning a grid near the honeycomb discharge might enhance turbulence decay (Scheiman 1981; Farell and Youssef 1996; Kulkarni et al. 2010). Grid-generated turbulence has been thoroughly studied by, for example, Laws and Livesey (1978); Comte-Bellot and Corrsin (1966) and Tan-Atichat et al. (1982), and is known to decay in two separate regions (Isaza et al. 2014). Various studies attempted to predict the decay behavior of grid-generated turbulence by a power law (Mohamed and Larue 1990; Kurian and Fransson 2009), but for honeycomb-grid generated turbulence, this remains a challenging task.

Loehrke and Nagib (1976) investigated the flow downstream of honeycombs with hydraulic cell diameter D_h and lengths $5.6 < L/D_h < 56.2$, followed by a grid with a solidity of 0.28. For all honeycombs considered in this study, introducing a grid near the discharge drastically reduced the level of turbulence and enhanced flow uniformity. As long as the grid was positioned upstream of the onset of the large-scale honeycomb-induced instabilities, a near-complete loss of influence of the honeycomb length on the downstream turbulence was observed. The authors argued that this is related to replacing the large-scale turbulence with smaller scales that are much more rapidly dissipated. For the shortest honeycomb considered in their study, the optimal offset between the discharge and grid was between $0 < x/D_h < 6$, where x is the streamwise distance from the honeycomb discharge, which increased with increasing honeycomb length. The authors argued that, since longer honeycombs have more developed flows at their discharge, longer distances are required to develop the large-scale instabilities so that the grid must be positioned further downstream for effective turbulence reduction. Finally, the authors mentioned that the turbulence downstream of a

honeycomb-grid combination is characteristic of neither of the original devices nor the superposition of the separate effects.

Scheiman (1981) investigated how a grid affects the flow downstream of honeycombs with lengths $6 < L/D_h < 8$. In contrast to Loehrke and Nagib (1976); Scheiman (1981) positioned the grid such that the honeycomb-generated turbulence was almost entirely dissipated before encountering it. He found that the turbulence reduction of a grid downstream of a honeycomb is far better than that of a grid alone. Furthermore, he argued that a honeycomb-grid combination is particularly effective in reducing turbulence since the turbulence downstream of a honeycomb is mainly axial, which grids are most capable of reducing. When a honeycomb was used alone or with a grid, the lateral turbulence was reduced more than the axial turbulence, while a grid alone reduces axial turbulence more than lateral turbulence. Finally, Scheiman (1981) mentioned that the inclusion of additional grids further reduces the turbulence intensity, but the first grid is more effective than the successive ones. Groth and Johansson (1988) found that for efficient turbulence reduction, the spacing between successive grids should be at least the length of the initial region of decay.

Farell and Youssef (1996) also investigated the effect of multiple grid downstream of honeycombs. They investigated honeycombs with lengths $8.5 < L/D_h < 42.7$, followed by a coarse grid with a solidity of 0.32 and two finer grids with solidities of 0.29 and 0.33. They found that the inclusion of a coarse screen near the discharge generally improves the performance of a honeycomb, and no substantial differences were observed between honeycombs of different lengths, which was also found by Loehrke and Nagib (1976). The honeycombs followed by both a coarse and a fine grid showed improved flow uniformity and significantly lower turbulence intensity than those without grids. They found that the inclusion of more fine grids further reduces the turbulence intensity at the cost of an increased pressure drop. Finally, the authors stated that in order to reduce large-scale swirling fluid motion and turbulence with short honeycombs, a coarse screen should be installed upstream of the honeycomb so that the flow reaching the inlet is as uniform as possible.

Finally, Kulkarni et al. (2010) numerically studied a honeycomb-grid combination using the k-ϵmodel. They found that the inclusion of a grid significantly improves the velocity uniformity at the cost of an increased pressure drop. Furthermore, a grid significantly reduces the turbulence intensity, which is associated with changing the large-scale turbulence to a more rapidly decaying smaller scale.

All the aforementioned experimental studies are conducted using hot-wire anemometry (HWA). This technology accurately measures properties of interest at specific points in space over a certain period, but is unable to obtain coherent information of larger flow fields in a single measurement. The present research presents novel insights into the effect of a grid on the evolution of honeycomb-generated turbulence by using 2D-planar PIV, which to the best of our knowledge, is the first study to do so. The main advantage of 2D-planar PIV over HWA is that entire flow fields can be captured on a near-instantaneous timescale, which enables the calculation of derivatives of the velocity and provides the possibility to correlate velocities at different points in space. However, this comes at the cost of a lower temporal resolution and therefore limited access to relevant turbulence properties, such as a fully resolved energy spectrum and the Kolmogorov length scale.

The present paper starts by investigating how the inclusion of a grid near the honeycomb discharge affects the streamwise evolution of the turbulence intensity, velocity and isotropy, as well as their vertical distributions over the height of the honeycomb. The experiments are conducted for two honeycombs of different lengths with both a laminar and a turbulent discharge.

2 Methodology

2.1 Particle image velocimetry

As mentioned above, the measurement technique is 2D-planar PIV due to its ability to capture entire flow fields on a near-instantaneous timescale. To obtain accurate results, it is crucial that the size of individual interrogation windows is tailored to the average particle displacement. Based on detailed studies of Thijs (2020) and Thijs et al. (2021) on the number of filtered vectors as a function of window size and average particle displacement, the present study uses an initial pass with interrogation windows with a size of 64×64 pixels and an overlap of 50%. Afterward, four additional passes are performed with a window size of 32×32 pixels and an overlap of 50%. The optimal number of image pairs remains a subject of debate since using more image pairs significantly increases computational expenses. In the present study, 800 image pairs are used after which the results are filtered with a second-order Savitzky–Golay filter to reduce experimental noise.

2.2 Experimental setup

The experiments are conducted in a single-channel wind tunnel made of Perspex with an internal height of 50 mm and a width of 70 mm, as illustrated in Fig. 1. The tunnel has a total length of 1.75 m and is composed of four individual sections.

An Elektror RD10/FUK variable flow pump forces ambient air through a dust filter into the tunnel.

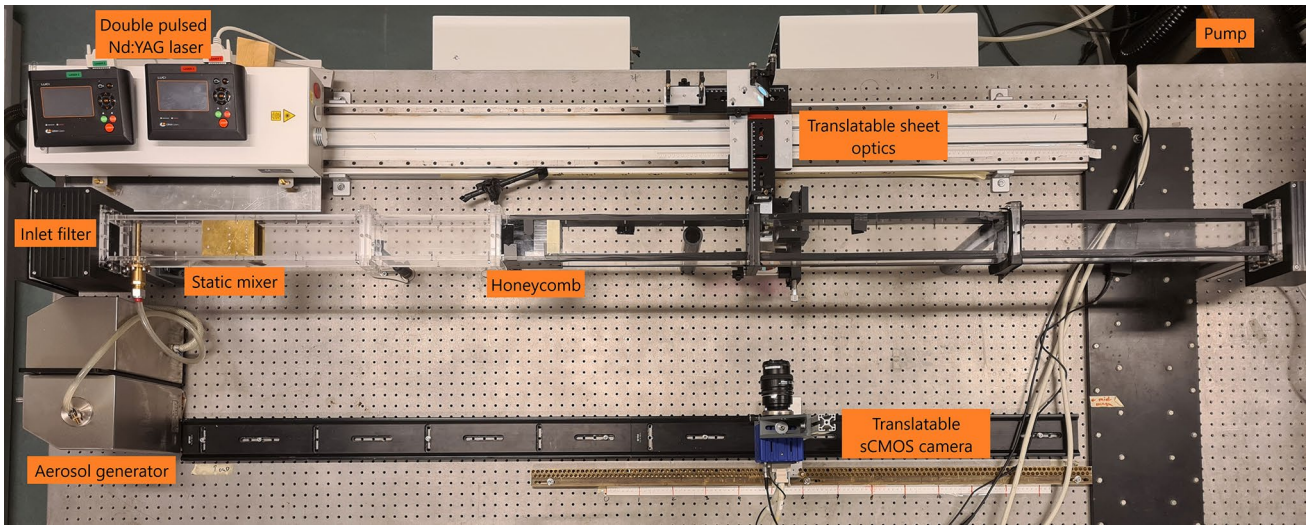

Fig. 1 Experimental setup

Di-ethyl-hexyl-sebacate (DEHS) aerosols with a mean diameter of 1 µm are injected into the flow in the streamwise direction, which are generated by a Palas AGF 2.0 Aerosol generator at a pressure of 2 bar. A static mixing device downstream of the injection zone ensures a homogeneous distribution of aerosols before the flow is laminarized by a 3D-printed honeycomb. After passing through the honeycomb, the aerosols are illuminated by a Litron Nano L 100-50 PIV pulsed Nd:YAG laser at a trigger rate of 15 Hz. The laser beam is deflected through sheet optics so that a 4-mm wide light sheet illuminates a section of the tunnel with its plane of symmetry in the z-direction. The laser emits pulses of 4 nanoseconds at the second harmonic frequency of 532 nm so that the attenuator must be reduced to 0.1% to prevent optical breakdown in the sample. The positions of the illuminated tracer particles are captured with a max 25 Hz 5.5-megapixel LaVision Imager sCMOS camera with a resolution of 2600 × 2200 pixels, equipped with a Nikon AF Nikkor 50 mm f/1.4D lens. This results in a field of view of 80 × 50 mm in the stream- and span-wise directions, respectively. Traverse systems ensure consistent camera and sheet optics translation between individual measurements and a LaVision VZ17-0690 programmable timing unit controls pulse and image timing. All measurements are conducted and processed with v10.1.2 of LaVision's DaVis and are post-processed with the PiVMat 4.0.1 toolbox in MATLAB R2020b.

2.3 Honeycombs and grid

Figure 2 illustrates a schematic frontal view of the used thick-walled honeycombs. The outer dimensions of the honeycombs are $H = 49.7$ mm and $W = 70$ mm, which are

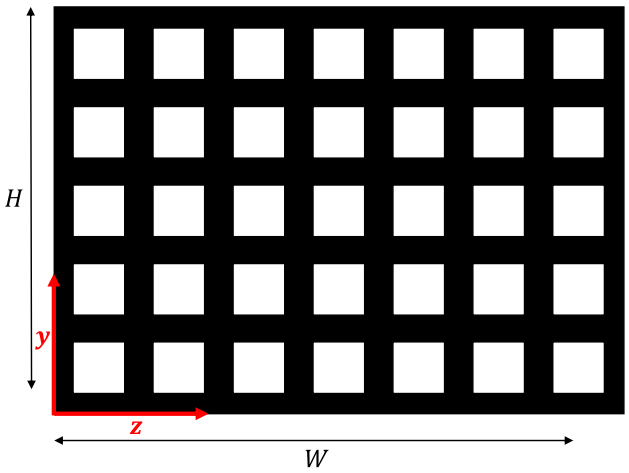

Fig. 2 Schematic frontal view of a thick-walled honeycomb

identical to the inner dimensions of the wind tunnel. Honeycomb 1 (HC1) has a length of $L = 50$ mm, a hydraulic diameter of $D_h = 6.35$ mm, a wall thickness of $t = 3.2$ mm and a solidity of $s = 0.61$. Honeycomb 2 (HC2) is fully identical to HC1, apart from having a length of 300 mm. The solidity of the honeycombs relates the mean ($\overline{U}_\infty$) and cell velocity ($\overline{U}_{\text{cell}}$) through the conservation of mass as

$$\overline{U}_{\text{cell}} = \frac{\overline{U}_\infty}{1 - s}. \tag{1}$$

Furthermore, a cell Reynolds number is introduced based on the hydraulic diameter of an individual honeycomb cell so that honeycombs with different cell sizes can be compared in a meaningful way. In the remainder of this work, the cell

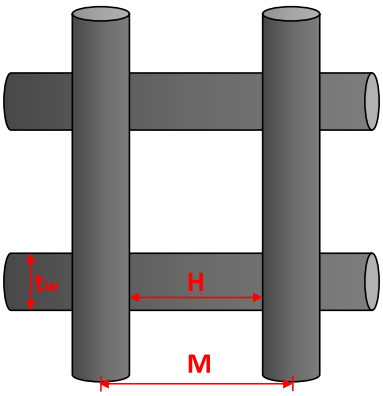

Fig. 3 Schematic frontal view of a section of the grid

Reynolds number is referred to as the Reynolds number unless specifically stated otherwise. The cell-based Reynolds number is given by

$$\mathrm{Re}_{\mathrm{cell}} = \frac{\overline{U}_{\mathrm{cell}} D_{\mathrm{h}}}{\nu}. \tag{2}$$

A section of the grid is schematically represented in Fig. 3. The grid has a solidity of $s = 0.48$ and a wire thickness of $t_w = 0.2$ mm. The mesh length M is calculated from the solidity and wire thickness as $M = \frac{t_w}{1-\sqrt{1-s}}$. From the mesh length and wire thickness, the gap size H is calculated as $H = M - t_w$. The grid can be mounted at various distances from the honeycombs with multiple metal rods and has outer dimensions equal to those of the honeycombs, e.g., a height and width of 49.7 mm and 70 mm, respectively.

2.4 Assumptions

Since 2D-planar PIV only measures in a 2-dimensional plane, information on the out-of-plane component is absent. Therefore, in the remainder of this study, it can be assumed that the mean velocity component in the z-direction ($\overline{w}$) and the derivatives of other components with respect to z are zero, since the measurements are conducted in a plane of symmetry that is perpendicular to the z-direction. Secondly, we assume isotropy of the velocity fluctuations in the y and z-directions, such that $v' = w'$. Under those assumptions, the turbulence intensity (TI) is calculated as

$$TI = \frac{\sqrt{\frac{1}{3}(\overline{u'^2} + 2\overline{v'^2})}}{\overline{U}_{\infty}}. \tag{3}$$

3 Results

In this chapter, we present our experimental findings on the impact of a grid when positioned near the discharges of HC1 ($L = 50$ mm) and HC2 ($L = 300$ mm). The streamwise evolution of TI and the fluid velocity are studied for both a laminar and a turbulent honeycomb discharge at Reynolds numbers 1850 and 3500, after which the spatial velocity correlation function and the axial and the lateral contributions to the turbulence are investigated. Finally, this chapter elaborates on the relevance of honeycomb length when utilized in a honeycomb-grid combination.

3.1 A grid near a laminar honeycomb discharge

This section illustrates the impact of a grid with a solidity of 0.48 near the discharges of HC1 and HC2 at cell Reynolds number 1850. Experiments revealed that both honeycombs have a laminar discharge at this Reynolds number, but the flow at the discharge of HC2 is *nearly* fully developed, whereas that at the discharge of HC1 is not. Even though HC2 is shorter than the hydrodynamic entrance length, it is known that the velocity profile rapidly develops in a small region near the channel inlet and only marginally in the remainder of the entrance length (Han 1960). Unless specifically mentioned otherwise, the data presented in this section are retrieved along a centerline through the center cells of the honeycombs, respectively at $y/D_{\mathrm{h}} = 0$ in the channel.

3.1.1 Streamwise evolution of the TI and velocity

Figure 4 illustrates the streamwise evolution of TI downstream of the grid when mounted at various distances (x)

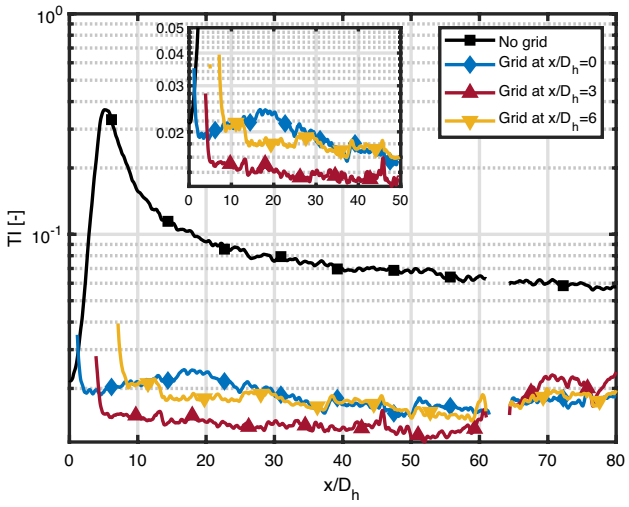

Fig. 4 Streamwise evolution of TI for a grid mounted at various distances from the discharge of HC1

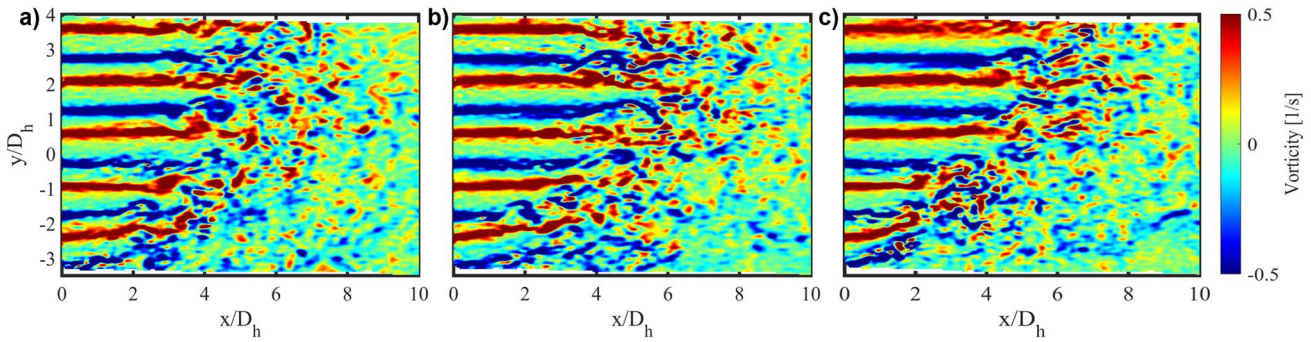

Fig. 5 Instantaneous vorticity downstream of HC1 at Reynolds number 1850, calculated as $w_z = \frac{\partial v}{\partial x} - \frac{\partial u}{\partial y}$. Figures *a*, *b* and *c* represent the first three frames, respectively, captured at a temporal resolution of 25 Hz, clearly illustrating the onset of instabilities near $x/D_h = 4$. Note that the temporal resolution is insufficient to capture the smallest time scales

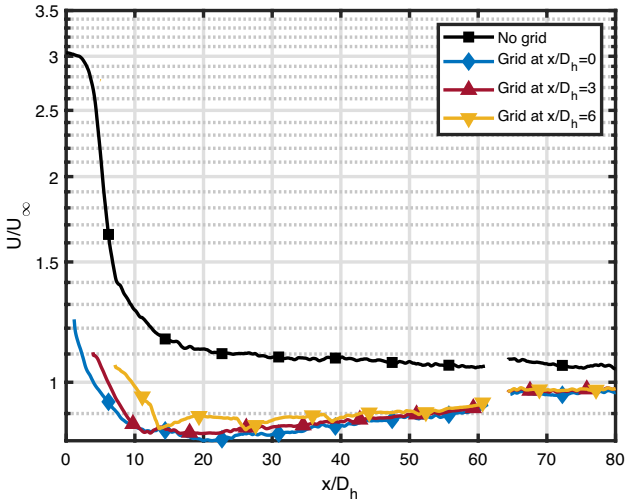

Fig. 6 Streamwise evolution of the axial velocity component for a grid mounted at various distances from the discharge of HC1

to the discharge of HC1. The profiles are only visualized downstream of the grid since laser-induced reflections limit the measurement accuracy in the region between the grid and honeycomb discharge. The same holds for the blank region near $x = 62D_h$, where the presence of a tunnel flange leads to over-illumination of the measurement region. The figure illustrates the remarkable impact of a grid when placed downstream of a honeycomb. The presence of the grid drastically reduces *TI* at any streamwise position and inhibits peak formation, regardless of its distance from the honeycomb discharge. Even though the difference in *TI* for varying grid positions is only marginal, *TI* shows a small local maximum near $x = 18D_h$ if the grid is mounted directly at the honeycomb discharge. The increase of *TI* upstream of this maximum could be related to the fact that the grid is positioned upstream of the onset of the large-scale instabilities. These instabilities arise from the merging of the shear layers that are formed in each honeycomb cell (Thijs et al. 2021) and the high-vorticity regions that are formed behind the honeycomb cell walls, as shown in Fig. 5. Especially near the bottom of the channel, the jets stemming from the honeycomb cells are highly disturbed, since a vortex that is induced by the static mixer has not yet been dissipated by the honeycomb. Since both the shear stresses and vorticity increase with honeycomb length, larger instabilities are formed downstream of longer honeycombs resulting in higher *TI* and TKE-production. When the grid is placed too far upstream, new instabilities can still arise downstream of the grid, indicating that more distance is required before the imprint of the honeycomb can be fully removed by the grid. These arguments are supported by the absence of new instabilities once the grid is mounted further from the honeycomb discharge at either $3D_h$ or $6D_h$. Interestingly, a grid positioned downstream of the peak in *TI* (e.g., at $6D_h$) reduces *TI* to nearly the same level as when placed upstream of the peak. Of the investigated offsets between the honeycomb discharge and grid, a distance of $3D_h$ seems most effective for reducing turbulence and reduces *TI* from 37% to only 3% downstream of $6D_h$ from the discharge. Furthermore, mounting a grid near the honeycomb discharge leads to a consistently low *TI* over large downstream distances, which only increases beyond $60D_h$ due to the formation of tunnel boundary layers. However, even when the boundary layers affect the flow, *TI* downstream of a honeycomb-grid combination is merely 2%, while almost 7% without grid.

Figure 6 illustrates the streamwise evolution of the local average streamwise velocity component under equal flow conditions as in Fig. 4, where U_∞ is determined as the average velocity between $20 < x/D_h < 40$. The grid drastically affects the strong jets resulting from the high solidity of the honeycomb, whereas the velocity remains high for a short distance when only using a honeycomb, it immediately plummets downstream of the grid. Various grid positions lead to a nearly identical velocity evolution, apart from the

delayed onset of decay due to the increased offset between the grid and honeycomb discharge.

Since Fig. 4 shows that, of the investigated offsets, a distance of $3D_h$ between the honeycomb discharge and grid is most effective for reducing turbulence, this combination is investigated further and compared to the case of a honeycomb only in Figs. 7 and 8. The honeycomb structure is clearly recognized by the high-velocity jets that are interconnected by regions of low velocity behind the cell walls. While the strong jets stemming from the honeycomb cells persist until $7D_h$ from the discharge in the absence of a grid, the inclusion of the grid separates them into many smaller jets that are much more rapidly dissipated. Due to the increased dissipation rate, the honeycomb-grid combination leads to a much more uniform velocity distribution near the honeycomb discharge. When utilizing the honeycomb-grid combination, the flow is nearly uniform beyond $10D_h$ from the discharge, since u/U_∞ is close to one over the full height of the channel, whereas the flow is still highly non-uniform in the absence of a grid. Interestingly, the presence of the grid leads to the formation of additional jets downstream of the honeycomb cell walls, as observed near $y = 0.85D_h$ in Fig. 8, where there is only a very low velocity when using a honeycomb only. Furthermore, it is observed that without grid the lower jet is directed slightly upward, while the other jets are straight. This is related to an instability that arises in the static mixing device upstream of the honeycomb, and since the honeycomb is short, has not yet been dissipated at the honeycomb discharge. Further experiments revealed that this phenomenon disappears when using longer honeycombs, since the increased pressure drop over the length of the channel evenly distributes the flow over the individual cells. In Fig. 8, the region between $2 < x/D_h < 3.5$ is blank due to over-illumination of the metal grid.

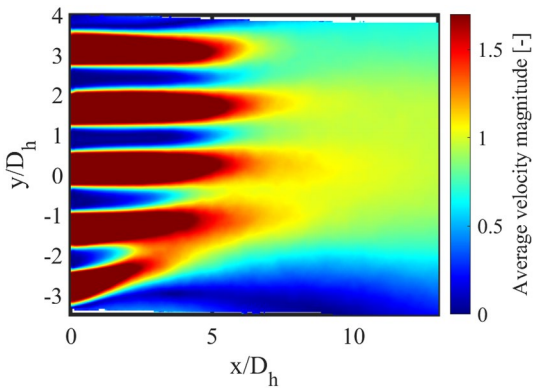

Fig. 7 Velocity distribution downstream of HC1 at Reynolds number 1850 in the z-center of the honeycomb

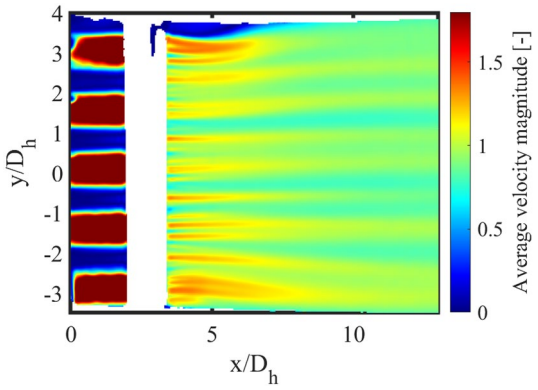

Fig. 8 Velocity distribution downstream of the HC1-grid combination at Reynolds number 1850 in the z-center of the honeycomb

3.1.2 Vertical distribution of *TI* and velocity

Next, Figs. 9 and 10 compare the vertical distributions of *TI* and the streamwise velocity directly downstream of the honeycomb-grid combination (at $x/D_h = 3$) to that at the same position when only using a honeycomb. When using a honeycomb-grid combination, *TI* is much more evenly distributed over the height of the channel, resulting in a *TI* between 3% and 10%, while that for a honeycomb only is between 10% and 50%. The maximum *TI* when using a grid is observed downstream of the honeycomb cell centers, but this maximum is close to the value of *TI* behind the cell walls as represented by the shaded rectangles. Furthermore, the additional turbulence from a vortex near the bottom tunnel wall in Fig. 9 is hardly visible when utilizing a honeycomb-grid combination. The velocity in Fig. 10 is nearly uniformly distributed at the surface of the grid, whereas the

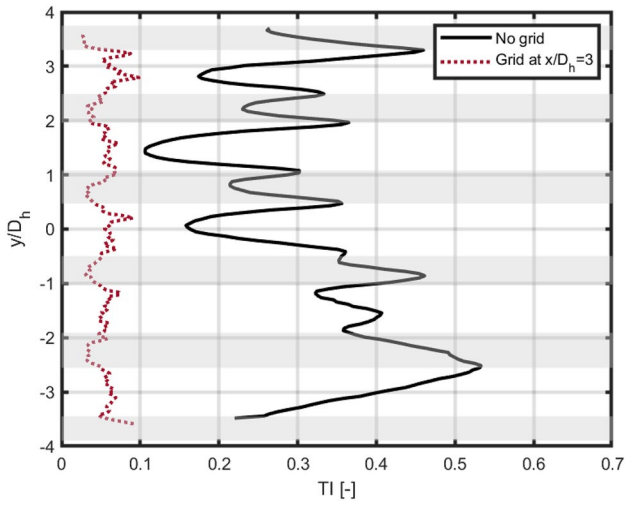

Fig. 9 Vertical distribution of *TI* at $x/D_h = 3$ at Reynolds number 1850 in the yz-center of the honeycomb

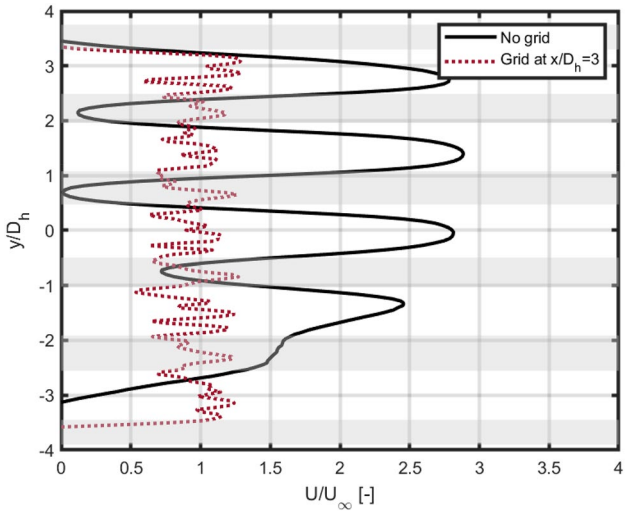

Fig. 10 Vertical distribution of the local average streamwise velocity at $x/D_h = 3$ at Reynolds number 1850 in the yz-center of the honeycomb

parabolic velocity profiles stemming from the individual cells are still clearly visible when using a honeycomb only.

3.1.3 Correlation length, integral length scale and energy spectrum

To gain further insight into how the turbulence is dissipated by a honeycomb grid combination, we introduce the spatial velocity correlation function R as

$$R(x_0, y_0, dx, dy) = \frac{\overline{u'(x_0, y_0, t)u'(x_0 + dx, y_0 + dy, t)}}{\overline{u'(x_0, y_0, t)u'(x_0, y_0, t)}}, \quad (4)$$

where (x_0, y_0) is a point of reference, dx and dy are the horizontal and vertical displacements with respect to (x_0, y_0) and u' is the local instantaneous velocity fluctuation calculated as $u' = u - \overline{u}$. The overbars indicate averaging over 800 image pairs. This correlation function can be used to calculate the integral length scale as $L_\lambda = \int_0^\infty R(x_0, y_0, dx, dy)d(dx)$, and to calculate the energy spectrum $E(k)$ as the Fourier transform of the correlation function.

Figures 11 and 12 illustrate 2D-correlation maps using $(x_0, y_0) = (4D_h, 0)$ and varying dx and dy over all possible positions in the field of view of the camera, for HC1 and the HC1-grid combination, respectively. This reference point is chosen such that its x-coordinate is located directly downstream of the grid and the y-coordinate at the center-height of the center cell of the honeycomb.

Figure 11 shows that, in the absence of a grid, the velocity downstream of the central channel has a higher correlation with the velocity downstream of the other channels than with the velocity downstream of the cell walls. The correlation

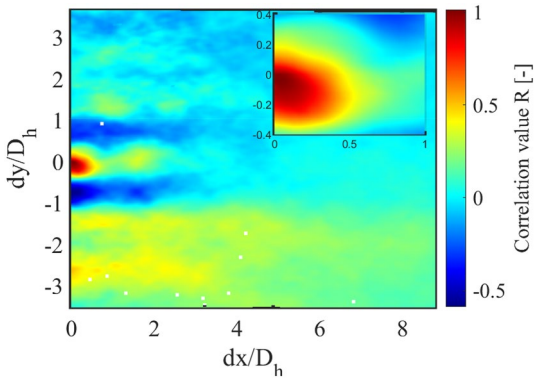

Fig. 11 Correlation map for the flow downstream of HC1 at Reynolds number 1850 with the point of reference located at $(x_0, y_0) = (4D_h, 0)$

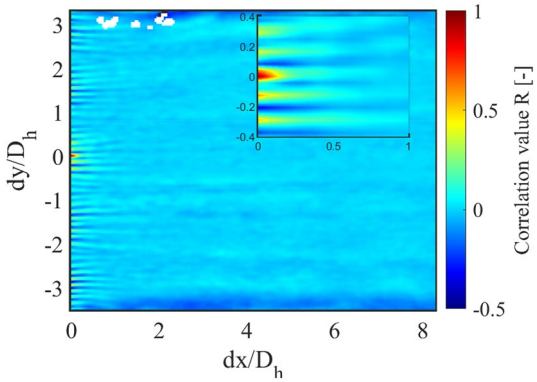

Fig. 12 Correlation map for the flow downstream of the HC1-grid combination at Reynolds number 1850 with the point of reference located at $(x_0, y_0) = (4D_h, 0)$

is higher for the bottom channels than for the top channels. This can be explained by the synchronous excitation of instabilities in the wakes of the cell walls. In general, the correlation function is slightly oriented toward the streamwise direction, which is caused by the larger streamwise velocity component. Interesting to note is the large negative correlation found between the reference point and points downstream of the neighboring cell walls. This points toward the circulating flow behind the cell walls. Figure 12 shows that even though the correlation function is still directed toward the streamwise direction when a grid is present, it decays much more rapidly and is nearly zero at $dx/D_h = 1$, whereas this takes a distance of nearly $5D_h$ without grid. The figure also illustrates that the grid helps to evenly distribute the flow over the height of the channel, since the correlation values near the small channels created by the wires of the grid are similar and the effect of the instability caused by the upstream mixer is absent. Furthermore, whereas it takes nearly $0.5D_h$ to reach $R < 0.5$ without grid,

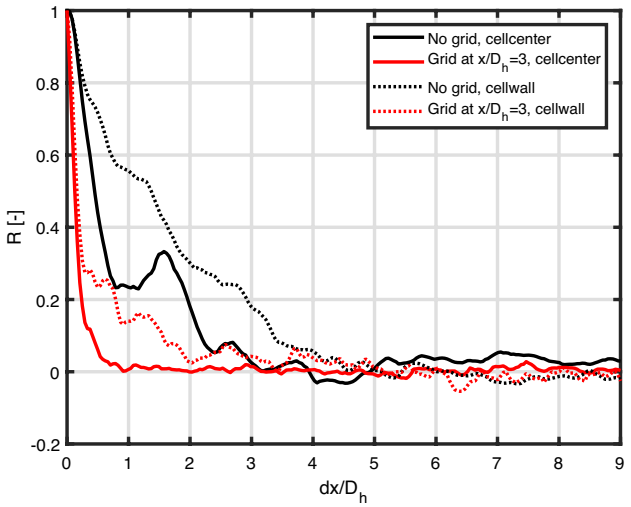

Fig. 13 Streamwise evolution of the correlation function for HC1 with and without grid at Reynolds number 1850, downstream of a honeycomb cell center ($y_0 = 0$) and a cell wall ($y_0 = 0.85D_h$)

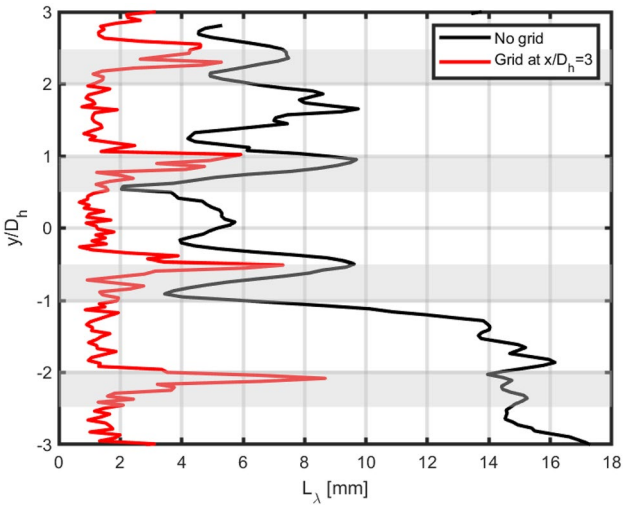

Fig. 14 The integral length scale as a function of the vertical coordinate with and without grid at $x = 3D_h$ and at Reynolds number 1850. The shaded rectangles represent the positions of the honeycomb cell walls at the honeycomb discharge

this merely requires $0.15D_h$ with grid, showing that a grid enhances the dissipation of turbulence by nearly a factor of three. Of particular interest is the large differences in correlation when the reference point is taken either downstream of the honeycomb cell centers or the honeycomb cell walls, as illustrated in Fig. 13.

Without grid, R remains nearly twice as large over the full downstream distance behind the cell walls than behind the cell centers. Furthermore, the correlation coefficient downstream of the honeycomb cell center decays much more rapidly than behind the cell walls, reaching $R = 0$ after only $3D_h$, whereas a distance of $5D_h$ is required downstream of the cell walls. When adding a grid at $x/D_h = 3$, a remarkable reduction of R is observed, downstream of both the cell centers and the cell walls. Very close to the grid, the correlation coefficients behind the cell walls and centers are similar, but R behind the cell centers reaches zero much faster, namely after only $1D_h$, whereas nearly $3D_h$ is required to reach $R = 0$ behind the cell walls. Even though the grid increases the reduction of R behind both the cell walls and cell centers, their difference is less than without a grid, therewith showing an enhancement of the flow distribution by the grid. The fully spatially resolved correlation function enables the calculation of the height-dependent integral length scale $L_\lambda(y_0)$ by integrating R between $dx = 0$ and the value of dx at which the correlation value first reaches zero, i.e., at $(x_0 + dx, y_0)\|_{R=0}$, for every possible y_0 in the channel. In the present study, the upper integration bound $(x_0 + dx)\|_{R=0}$ is preferred over the limiting case where $dx \to \infty$ to limit the influence of experimental noise that becomes more significant when the correlation value approaches zero. Figure 14 illustrates the integral length scale at various vertical

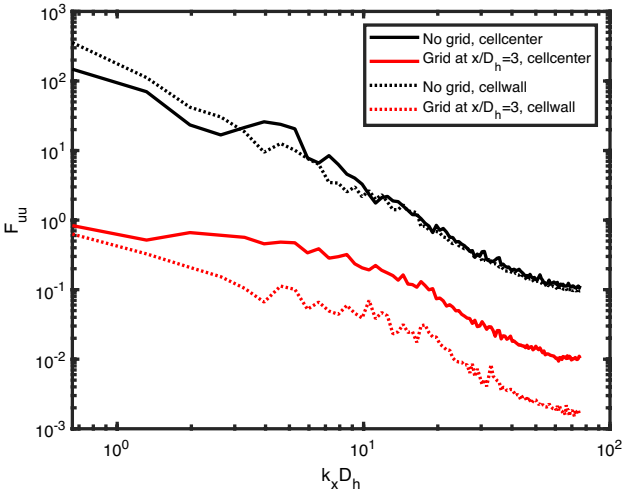

Fig. 15 Energy spectrum in the axial direction for HC1 at Reynolds number 1850

positions in the channel with and without grid. It is clear that the grid drastically reduces L_λ over the full height of the channel. Even though the peak magnitudes of L_λ downstream of the cell walls are still substantially larger than downstream of the cell centers when using a grid, they are much sharper so that the resulting large-scale instabilities are much more rapidly dissipated than without a grid. While the magnitudes of the peaks downstream of the cell walls with and without grid are somewhat similar, L_λ reduces by nearly a factor 10 from 18 mm to 1.8 mm near $y = -3D_h$, stemming from the enhanced flow uniformity over the grid

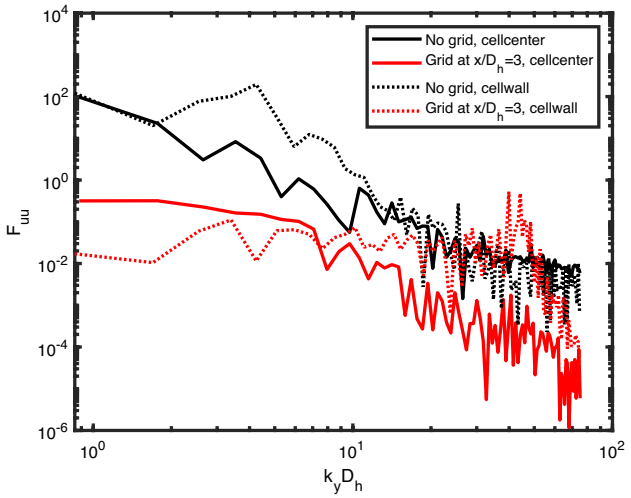

Fig. 16 Energy spectrum in the lateral direction for HC1 at Reynolds number 1850

so that the effect of the mixer-induced instability becomes less pronounced.

Besides calculation of the integral length scale, the spatial velocity correlation function is also used to calculate the axial and lateral energy spectra $F(k)$ by applying a Fourier transform. These energy spectra provide insight into the distribution of energy over the various wave numbers and thus describe the contribution of particularly sized eddies to the turbulence kinetic energy production. Figures 15 and 16 show the axial and lateral energy spectra for HC1 at Reynolds number 1850, where x_0 remains fixed at $x = 3D_\mathrm{h}$ and y_0 is set to the height of either the cell wall or the cell center. Note that wave number k is related to wavelength λ as $k = 2\pi/\lambda$. The grid downstream of the honeycomb drastically reduces the axial and lateral energy contained in eddies with smaller wave numbers by up to a factor 10^2, regardless of whether the reference height is taken near a cell wall or a cell center. This large reduction stems from the small thickness of the wires compared to that of the cell walls, so that the large-scale eddies generated by the high solidity of the honeycomb are broken up into many smaller regions that contain mostly small-scale instabilities. Furthermore, this confirms our previous observation that a grid leads to near-instantaneous decay of the turbulence intensity, since the contribution of the large-scale instabilities with low wave numbers is reduced by nearly a factor 100. While our expectation that changing the reference height from that of the cell center to that of the cell wall increases the axial and lateral energy contained in the smaller wave numbers is affirmed, the opposite holds when using a grid downstream of the honeycomb. The latter might originate from the small thickness of the wire so that both small and large eddies are nearly absent very close to the wires. Also interesting to note is that when the reference height is taken as that downstream of the cell wall, using a grid leads to a larger lateral contribution of the smaller wave numbers than when the reference point is taken at the center height of the central channel. This agrees with our previous observations and confirms that the grid converts the large-scale instabilities into smaller scales.

Finally, it is surprising to note that all spectra contain a peak near $kD_\mathrm{h} = 4$. These peaks stem from the geometry of the honeycomb and are directly related to the distance between the individual channels. Since wavelength λ and wave number k are related via $\lambda = 2\pi/k$, the point where $kD_\mathrm{h} = 4$ corresponds to a wavelength of $\lambda = 1.5D_\mathrm{h}$. Considering that the hydraulic cell diameter and wall thickness are $1D_\mathrm{h}$ and $0.5D_\mathrm{h}$, respectively, and that their sum is thus $1.5D_\mathrm{h}$, the wavelength resulting from the geometry of the honeycomb exactly corresponds to the peaks in the energy spectra.

3.1.4 Turbulence contributions

Apart from affecting the total degree of turbulence in the flow, Fig. 17 illustrates how the individual contributions to the turbulence are affected by a grid downstream of the honeycomb discharge. In contrast to a honeycomb only, which mainly inhibits lateral turbulence (Scheiman 1981), the honeycomb-grid combination inhibits both the axial and lateral contributions, regardless of the offset between the grid and honeycomb discharge. The axial contributions remain more prominent than the lateral ones due to the much larger velocity magnitude in the axial direction. Similar results were obtained by Scheiman (1981), who also mentioned that the axial contributions dominate over the lateral downstream of honeycomb-grid combinations. Further investigations

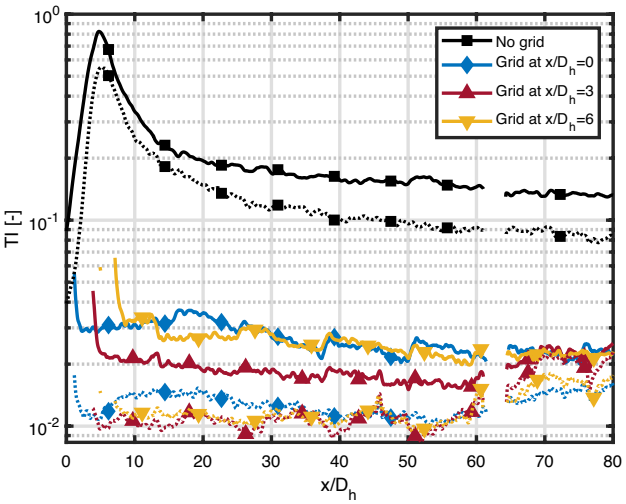

Fig. 17 Axial and lateral contributions to the turbulence at Reynolds number 1850 in the *yz*-center of the honeycomb. The solid and dashed lines represent the axial and lateral contributions, respectively

revealed that the anisotropy increases near the honeycomb discharge when using a grid, but this is most likely related to the rapidly decreasing order of magnitude of the individual contributions.

3.1.5 Honeycomb length

Finally, we investigate how the honeycomb length affects the performance of a honeycomb-grid combination with a laminar honeycomb discharge. Therefore, the combinations of HC1 ($L = 50$ mm) and HC2 ($L = 300$ mm) with a grid at $3D_h$ from their discharge are compared at Reynolds number 1850 and their velocity distributions are illustrated in Figs. 18 and 19. Since HC2 has a more developed flow at its discharge due to its larger length, the high-velocity jets stemming from the individual cells are more persistent than those of HC1 and are less evenly distributed over the height of the grid. The grid near the discharge of HC2 primarily separates the strong jets into smaller ones, but these smaller jets remain of high velocity and persist further downstream of the grid than for a short honeycomb. This suggests that the optimal grid position shifts in the streamwise direction when increasing honeycomb length since the more developed jets stemming from longer honeycomb channels require more downstream distance before reaching the onset of the large-scale instabilities. These findings agree with those of Loehrke and Nagib (1976), who mentioned that the optimal position of a grid increases in the streamwise direction for increasing honeycomb length.

Figures 20 and 21 compare the streamwise evolution of *TI* and the streamwise velocity when using honeycombs of different lengths, with and without a grid. The profiles are again visualized along a centerline through the center cell

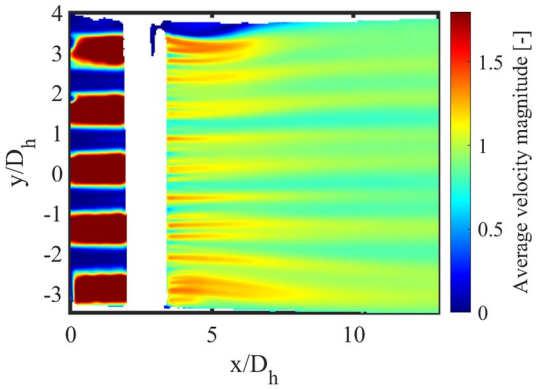

Fig. 18 Velocity distribution downstream of the HC1-grid combination at Reynolds number 1850 in the *z*-center of the channel

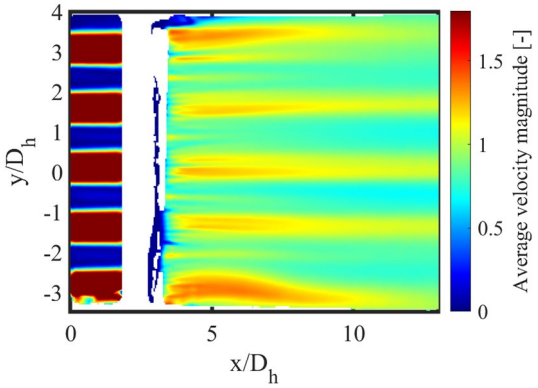

Fig. 19 Velocity distribution downstream of the HC2-grid combination at Reynolds number 1850 in the *z*-center of the channel

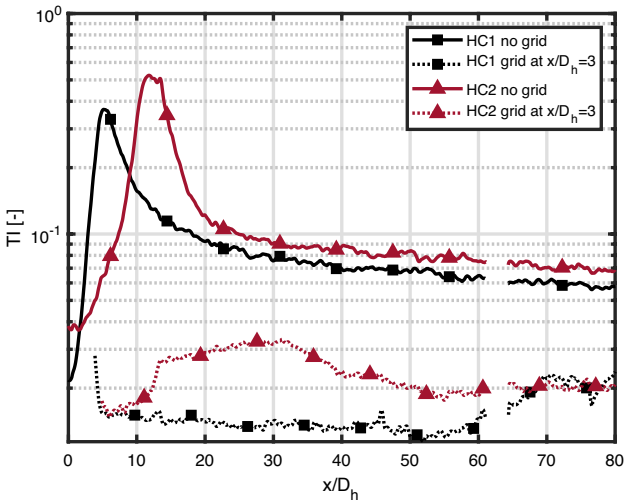

Fig. 20 Streamwise evolution of *TI* downstream of HC1 and HC2 with and without grid at Reynolds number 1850 in the *yz*-center of the honeycomb

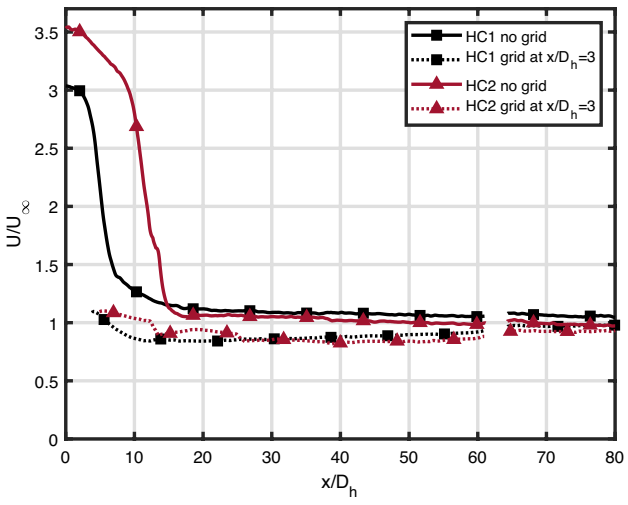

Fig. 21 Streamwise evolution of the streamwise velocity downstream of HC1 and HC2 with and without grid at Reynolds number 1850 in the *yz*-center of the honeycomb

of the honeycomb. Independent of the honeycomb length, including a grid drastically reduces *TI* and enhances flow uniformity. Even though the longer honeycomb produces more turbulence than the short one due to the larger length-scale of the shear layers, the utilization of a grid results in a near-complete loss of the influence of the honeycomb length on the turbulence production downstream of the HC-grid combination, as also mentioned by Loehrke and Nagib (1976). *TI* remains consistently low when the grid is combined with HC1 but slightly increases near $x = 10D_h$ when combined with HC2 before it decays to the same level as HC1. This once again results from the larger length scale of the shear layers for a longer honeycomb so that a larger offset between the honeycomb discharge and grid is required to achieve effective turbulence reduction.

In summary, we conclude that installing a grid near a laminar honeycomb discharge drastically reduces both the axial and the lateral turbulence and improves flow uniformity, at the cost of an additional pressure drop over the grid. The distance between the honeycomb discharge and grid at which the grid most effectively reduces the honeycomb-generated turbulence seems to increase with honeycomb length, but further research is required to study the relation between the two. Even though the longer honeycomb more effectively distributes the flow over the channel, increasing the honeycomb length from 50 to 300 mm simultaneously increases the pressure drop from 124 to 742 Pa and can thus be detrimental for applications that require minimal pressure losses. Finally, installing a grid near a honeycomb discharge leads to a near-complete loss of influence of the honeycomb length on the production of honeycomb-generated turbulence, as long as it is positioned correctly.

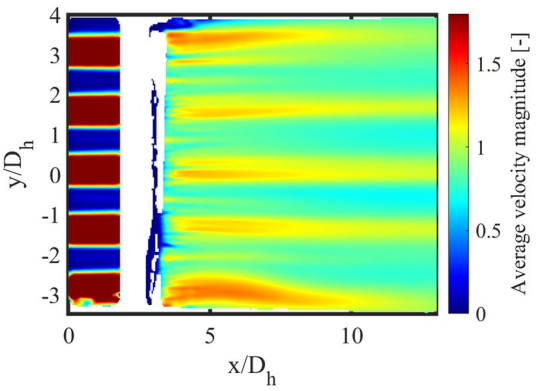

Fig. 22 Velocity distribution downstream of the HC2-grid combination at Reynolds number 1850 in the *z*-center of the channel (laminar)

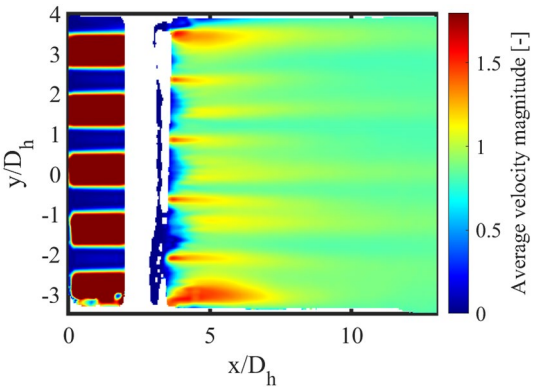

Fig. 23 Velocity distribution downstream of the HC2-grid combination at Reynolds number 3500 in the *z*-center of the channel (turbulent)

3.2 A grid near a turbulent honeycomb discharge

In the previous section, both honeycomb-grid combinations had laminar flow at the honeycomb discharge. In this section, a honeycomb-grid combination with a laminar honeycomb discharge is compared to the same combination with a turbulent discharge. Therefore, the grid is mounted with an offset of $3D_h$ to HC2 and studied at Reynolds numbers 1850 and 3500, which were found to result in respectively a laminar and a turbulent discharge.

Figures 22 and 23 illustrate the distributions of the local average streamwise velocity downstream of the HC2-grid combination at Reynolds numbers 1850 and 3500. The high-velocity jets stemming from the individual honeycomb cells are much more persistent when the honeycomb discharge is laminar, but rapidly dissipate when the discharge is turbulent. The maximum velocity is observed downstream of the honeycomb cell centers when the discharge is laminar, whereas it is found behind the cell walls when the discharge is turbulent. Furthermore, the velocity shows a much more even distribution downstream of the grid when the discharge is turbulent, resulting from the increased rate of dissipation of the large-scale instabilities.

As illustrated in Figs. 24 and 25, with both a laminar and turbulent discharge, the highest *TI* downstream of the grid is found at the heights of the honeycomb cell centers, clearly indicating that the flow is not yet uniformly distributed at the location of the grid. The region between the honeycomb discharge and grid is highly influenced by laser-induced reflections, so the visualization between $0 < x/D_h < 3$ is not reliable and should not be taken into consideration. Downstream of the grid, *TI* is higher near the cell walls for a turbulent honeycomb discharge and the turbulence from the three inner cells is much more rapidly dissipated. While the individual wakes from the grid are still visible at $x = 12D_h$ for a laminar discharge, they are not for a turbulent discharge. These findings suggest that the grid should be positioned further downstream for a laminar discharge than for a turbulent discharge since the transition to turbulent flow shifts

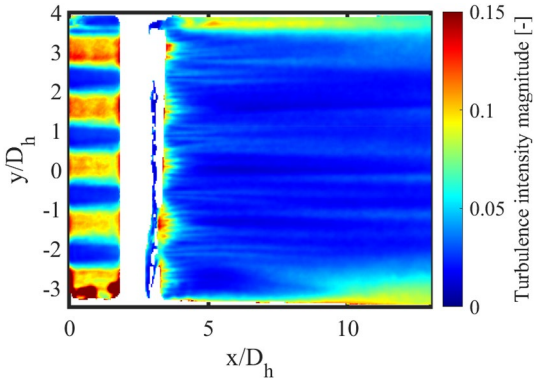

Fig. 24 Distribution of *TI* downstream of the HC2-grid combination at Reynolds number 1850 in the *z*-center of the channel (laminar)

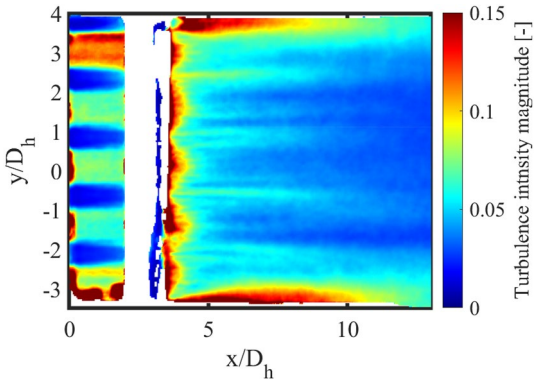

Fig. 25 Distribution of *TI* downstream of the HC2-grid combination at Reynolds number 3500 in the *z*-center of the channel (turbulent)

the position of peak *TI* and thus the onset of the large-scale instabilities upstream.

Next, Figs. 26 and 27 illustrate the evolution of *TI* and the streamwise velocity along a centerline through the center cells of the honeycombs. This figure clearly illustrates the transition to turbulence at Reynolds number 3500 by the large increase in *TI* (to nearly 13%) directly downstream of the discharge. Although it may seem that the laminar flow has a higher *TI* than the turbulent flow, it must be noted that the respective curves represent the dimensionless *TI*. Since the relative contribution of the fluctuations increases less rapidly than that of the mean velocity, increasing the Reynolds number leads to a lower dimensionless *TI*. The dimensional velocity fluctuations are larger for turbulent flow than for laminar flow. Even though a decreasing *TI* with increasing Reynolds number is usually not observed in channel flow, previous studies (Thijs et al. 2021) that investigated flows laminarized by honeycombs reported similar results. Even though the flows without a grid show significant differences between a laminar and a turbulent discharge, this difference almost entirely disappears when using a grid. *TI*

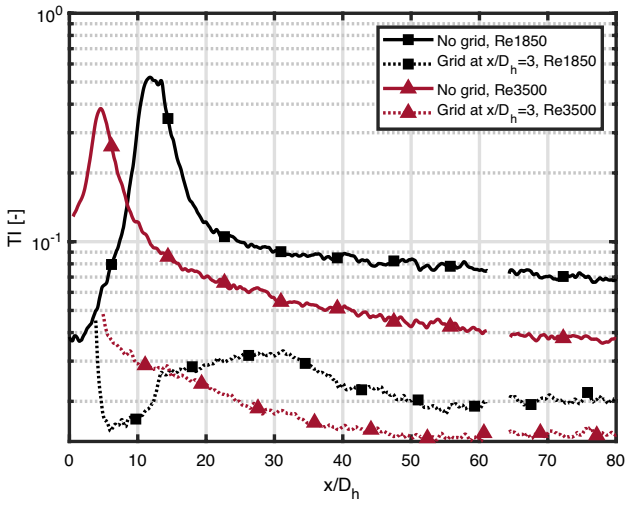

Fig. 26 Streamwise evolution of *TI* downstream of the HC2-grid combination for a laminar (Re1850) and a turbulent (Re3500) discharge in the *z*-center of the channel

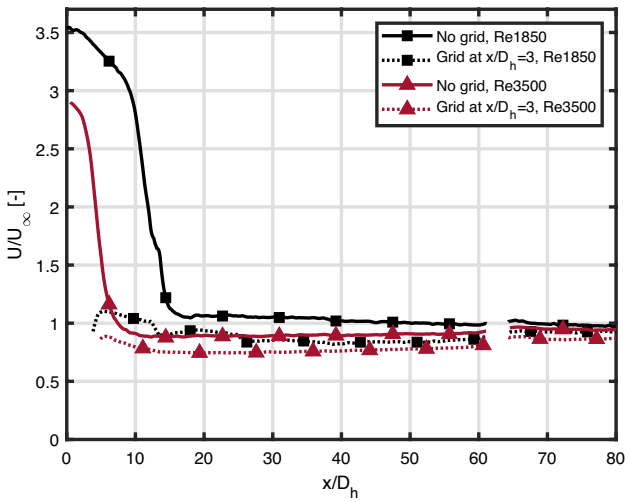

Fig. 27 Streamwise evolution of the streamwise velocity component downstream of the HC2-grid combination for a laminar (Re1850) and a turbulent (Re3500) discharge in the *z*-center of the channel

near the grid is slightly higher when the discharge is turbulent than when it is laminar, but the remaining turbulence is more rapidly dissipated. The increase in *TI* at Reynolds number 1850 near $x/D_h = 5$, together with the peak in *TI* being more downstream when not using a grid, indicates that the optimal grid position is related to the position of peak *TI*. The figure clearly illustrates that even though the difference between a laminar and a turbulent discharge with a grid is marginal, the grid position is not optimal for a turbulent discharge since *TI* slightly increases downstream of the grid. The flow is nearly uniform downstream of the grid

for both a laminar and turbulent discharge, but the velocity is slightly higher when the discharge is laminar due to the larger velocity in the center of the honeycomb cell.

From this section, we conclude that a grid effectively reduces turbulence and increases flow uniformity when placed slightly downstream of a turbulent honeycomb discharge. However, it must be noted that the pressure drop over the honeycomb-grid combination for the turbulent case is much larger since the pressure drop scales with the square of the velocity.

4 Conclusion

In the present study, 2D-planar PIV was used to investigate how honeycomb-generated turbulence is affected by a downstream grid with a solidity of 0.48. The research was conducted for both a short ($L = 50$ mm) and a long ($L = 300$ mm) honeycomb and for both a laminar and a turbulent discharge at cell Reynolds numbers 1850 and 3500. The grid separates the strong jets stemming from the honeycomb cells into many smaller jets that are much more rapidly dissipated, therewith drastically reducing the correlation length and enhancing flow uniformity. The spatial velocity correlation function is indicative of a circulating flow field near the honeycomb discharge when no grid was used, and can be drastically affected by placing a grid near the honeycomb discharge. Calculation of the height-dependent integral length scale showed a large reduction of average eddie size when using a grid and reduced the magnitude at the peak position from 18 to 1.8 mm. The energy spectra that are obtained by a Fourier transform of the spatial velocity correlation function show that a grid limits the contribution of the lower wave numbers and shows more large-scale instabilities downstream of the center wall than downstream of the central channel. Furthermore, the grid reduces peak turbulence intensity by up to 95% and inhibits both the axial and lateral contributions to the turbulence. The grid is most effective to reduce turbulence when there is a small distance between the grid and the honeycomb discharge due to the delayed onset of the large-scale instabilities in the wake of longer honeycombs. From our results, we conclude that a distance of $3D_h$ is most effective, but further studies are needed to investigate how the optimal distance is related to the honeycomb length and Reynolds number. Even though longer honeycombs produce more turbulence than short ones, the honeycomb length and turbulence production are almost entirely decoupled when a grid is placed near the honeycomb discharge. These results agree with previous research on honeycomb-grid combinations exposed to free-stream turbulence. The grid is extremely effective when placed near the discharge of both short and long honeycombs for both laminar and turbulent flows. Therefore, we conclude that a grid is extremely beneficial in many fluid-driven applications as it allows exploiting the benefits of longer honeycombs while maintaining small turbulence levels due to the grid. It would be interesting to confirm these experimental findings by numerical simulations.

Acknowledgements The authors wish to thank ir. L.C. Thijs for his support on numerical data analysis and G.W.J.M. Oerlemans and J. Baijens for their technical support.

Author contributions The authors contributions are as follows: NRMS conducting experiments, data processing, writing, and proofreading. JGMK performed supervision, outlining, and proofreading. JCHZ did supervision, outlining, and proofreading.

Funding This study was funded by the Eindhoven University of Technology.

Data availability All data can be provided by the main author upon request.

Declarations

Conflict of interest The authors have no competing or financial interests to declare that are relevant to the content of this article.

Consent for publication All authors give consent for publication

References

Comte-Bellot G, Corrsin S (1966) The use of a contraction to improve the isotropy of grid-generated turbulence. J Fluid Mech 25(4):657–682. https://doi.org/10.1017/S0022112066000338

Farell C, Youssef S (1996) Experiments on turbulence management using screens and honeycombs. J Fluids Eng 118(1):26–32. https://doi.org/10.1115/1.2817505

Groth J, Johansson A (1988) Turbulence reduction by screens. J Fluid Mech 197:139–155. https://doi.org/10.1017/S0022112088003209

Han L (1960) Hydrodynamic entrance lengths for incompressible laminar flow in rectangular ducts. J Appl Mech 27(3):403–409. https://doi.org/10.1115/1.3644015

Isaza J, Salazar R, Warhaft Z (2014) On grid-generated turbulence in the near- and far field regions. J Fluid Mech 753:402–426. https://doi.org/10.1017/jfm.2014.375

Kulkarni V, Sahoo N, Chavan S (2010) Simulation of honeycomb-screen combinations for turbulence management in a subsonic wind tunnel. J Wind Eng Ind Aerodyn 99(2011):37–45. https://doi.org/10.1016/j.jweia.2010.10.006

Kurian T, Fransson J (2009) Grid-generated turbulence revisited. Fluid Dyn Res 41(021):403. https://doi.org/10.1088/0169-5983/41/2/021403

Laws E, Livesey J (1978) Flow through screens. Ann Rev Fluid Mech 10(1):247–266. https://doi.org/10.1146/annurev.fl.10.010178.001335

Loehrke R, Nagib H (1976) Control of free-stream turbulence by means of honeycombs: A balance between suppression and generation. J Fluids Eng 98(3):342–351. https://doi.org/10.1115/1.3448313

Lumley J, McMahon J (1967) Reducing water tunnel turbulence by means of a honeycomb. J Basic Eng 89(4):764–770. https://doi.org/10.1115/1.3609700

Mikhailova N, Repik E, Sosedko YP (1994) Optimal control of free-stream turbulence intensity by means op honeycombs. Fluid Dyn 29:429–437. https://doi.org/10.1007/BF02230780

Mohamed M, Larue J (1990) The decay power law in grid-generated turbulence. J Fluid Mech 219:195–214. https://doi.org/10.1017/S0022112090002919

Scheiman J (1981) Comparison of experimental and theoretical turbulence reduction characteristics for screens, honeycomb, and honeycomb-screen combinations. NASA Technical Paper

Schipper N (2022) Experimental and numerical investigations on turbulence decay and particle behaviour in Magnetic Density Separation. Thesis, Eindhoven University of Technology, M.Sc

Tajfirooz S, Meijer J, Dellaert R et al (2021) Direct numerical simulation of magneto-archimedes separation of spherical particles. J Fluid Mech 910(1001):1–35. https://doi.org/10.1017/jfm.2020.1001

Tan-Atichat J, Nagib H, Loehrke RI (1982) Interaction of free-stream turbulence with screens and grids: a balance between turbulence scales. J Fluid Mech 114:501–528. https://doi.org/10.1017/S0022112082000275

Thijs L (2020) Honeycomb wake turbulence and particle dynamics in a magnetic density separation system. Thesis, Eindhoven University of Technology, M.Sc

Thijs L, Dellaert RA, Tajfirooz S et al (2021) Honeycomb-generated reynolds-number-dependent wake turbulence. J Turbul 22(9):535–561. https://doi.org/10.1080/14685248.2021.1932944